



Cite this: *Soft Matter*, 2019, 15, 9056

## Non-monotonic dependence of stiffness on actin crosslinking in cytoskeleton composites

Madison L. Francis,<sup>a</sup> Shea N. Ricketts,<sup>a</sup> Leila Farhadi,<sup>b</sup> Michael J. Rust,<sup>c</sup> Moumita Das,<sup>d</sup> Jennifer L. Ross <sup>b</sup> and Rae M. Robertson-Anderson \*<sup>a</sup>

The cytoskeleton is able to precisely tune its structure and mechanics through interactions between semiflexible actin filaments, rigid microtubules and a suite of crosslinker proteins. However, the role that each of these components, as well as the interactions between them, plays in the dynamics of the composite cytoskeleton remains an open question. Here, we use optical tweezers microrheology and fluorescence confocal microscopy to reveal the surprising ways in which actin crosslinking tunes the viscoelasticity and mobility of actin–microtubule composites from steady-state to the highly nonlinear regime. While previous studies have shown that increasing crosslinking in actin networks increases elasticity and stiffness, we instead find that composite stiffness displays a striking non-monotonic dependence on actin crosslinking – first increasing then decreasing to a response similar to or even lower than un-linked composites. We further show that actin crosslinking has an unexpectedly strong impact on the mobility of microtubules; and it is in fact the microtubule mobility – dictated by crosslinker-driven rearrangements of actin filaments – that controls composite stiffness. This result is at odds with conventional thought that actin mobility drives cytoskeleton mechanics. More generally, our results demonstrate that – when crosslinking composite materials to confer strength and resilience – more is not always better.

Received 1st August 2019,  
Accepted 15th October 2019

DOI: 10.1039/c9sm01550g

[rsc.li/soft-matter-journal](http://rsc.li/soft-matter-journal)

## Introduction

Cells are fascinating chemo-mechanical machines composed of smaller chemo-mechanical machines that span scales down to individual enzymes. Much of the mechanical nature of cells is conferred by the cytoskeleton, which provides support and viscoelasticity to cells to enable diverse processes such as migration, apoptosis and division.<sup>1</sup> More specifically, the wide-ranging mechanics that cells exhibit are largely enabled by networks of semiflexible actin filaments, along with actin crosslinking proteins, which are at the heart of essential biological processes like cytokinesis, contraction, morphological changes, neuronal development, *etc.*<sup>1–3</sup> Varying crosslinking patterns of actin have also been shown to underlie numerous pathologies by altering the mechanical properties of cells.<sup>2–5</sup>

To understand the role of actin crosslinking in cells, numerous studies have investigated the mechanical properties of crosslinked

actin networks *in vitro*.<sup>1,6–9</sup> These studies have shown that the majority of crosslinking proteins form isotropic networks of cross-linked filaments at low and intermediate crosslinker:actin monomer ratios,  $R$ , but form bundles of nematically aligned filaments at high  $R$ .<sup>8,10–12</sup> Due to these structural changes, increasing crosslinker concentrations have been shown to directly correlate with increased network stiffness and elasticity.<sup>1,8–10,12–16</sup> This intuitive result arises from permanent linkages between filament crossings or entanglements suppressing filament fluctuations and diffusive relaxation modes that allow networks to dissipate stress and exhibit mobility and plasticity.<sup>1,6</sup>

Although most of the viscoelastic mechanical properties exhibited by the cytoskeleton have been attributed to actin and its crosslinking proteins,<sup>2,3,6,7,9</sup> rigid microtubules are also key to the diverse mechanics that the cytoskeleton can exhibit. Moreover, the interactions between actin filaments and microtubules have been shown to drive essential cell functions such as navigation, intracellular trafficking, and mitotic spindle formation.<sup>17</sup> More generally, composites of stiff and flexible polymers have been shown to exhibit emergent viscoelastic properties desirable for industrial applications, such as low-weight and high-strength, stress-stiffening, and mechano-memory, that can be precisely tuned by the relative concentrations of and interactions between the constituents.<sup>14,18–20</sup>

However, despite the mounting evidence of the importance of actin-microtubule interactions to cytoskeleton mechanics

<sup>a</sup> Department of Physics and Biophysics, University of San Diego, 5998 Alcalá Park, San Diego, CA 92110, USA. E-mail: [randerson@sandiego.edu](mailto:randerson@sandiego.edu)

<sup>b</sup> Department of Physics, University of Massachusetts, Amherst, 666 N. Pleasant St., Amherst, MA 01003, USA

<sup>c</sup> Department of Molecular Genetics and Cell Biology, University of Chicago, 900 E 57th St, Chicago, IL 60637, USA

<sup>d</sup> School of Physics and Astronomy, Rochester Institute of Technology, 84 Lomb Memorial Drive, Rochester, NY 14623, USA

and function<sup>2,3,5,7,16,21</sup> – and the applicability to biomimetic materials design – how the presence of microtubules influences the mechanics of crosslinked actin networks remains largely unexplored.<sup>6,7</sup> Here, we directly address this important problem by characterizing the effect of actin crosslinking on the micro- and meso-scale mechanics and mobility of *in vitro* actin-microtubule composites.

We previously showed that actin-microtubule composites crosslinked by biotin-NeutrAvidin exhibit scale-dependent mechanics dependent on the type of crosslinking (actin-actin, microtubule-microtubule, or actin-microtubule).<sup>6</sup> Specifically, all crosslinking motifs increase the resistive force and stiffness of the composites and reduce filament mobility, but microtubule crosslinking is required for primarily elastic response. The subtle effect of actin crosslinking on composite mechanics that this study revealed begs the question as to the role of actin crosslinking in mechanics and its dependence on the crosslinking concentration.

Here, we use optical tweezers microrheology and fluorescence microscopy to map the linear and nonlinear rheological properties of actin-microtubule composites to the degree of actin crosslinking. Surprisingly, we find that beyond a critical crosslinker concentration the network stiffness and viscosity actually decrease to magnitudes comparable or even less than those for composites without crosslinkers. This counterintuitive non-monotonic dependence on crosslinker density persists from the steady-state to nonlinear regimes and from molecular to cellular scales. We show that this emergent phenomenon is dictated by the mobility of microtubules in composites, which is slowed the most when the actin network that scaffolds microtubules is both rigidly crosslinked and sufficiently dense. Too much crosslinking leads to actin bundling, thereby increasing the actin scaffold mesh size and thus allowing for more microtubule mobility. Conversely, too few crosslinks confer a dense but floppy scaffold that is insufficient to markedly suppress microtubule fluctuations. This careful balance demonstrates the elegant ways that actin crosslinking can modulate the interactions between actin and microtubules within the cytoskeleton to enable a myriad of different mechanical responses and processes in cells. More generally, this work reveals surprising design principles for biomimetic composite materials – showing that modest changes to filament interactions can lead to dramatic improvements in toughness and elasticity.

## Methods

Rabbit skeletal actin monomers (G-actin), biotinylated G-actin and Alexa-488-labeled G-actin are purchased from Cytoskeleton (AKL99, AB07) and Thermofisher (A12373) and suspended at 1 mg ml<sup>-1</sup>, 2 mg ml<sup>-1</sup> and 1.5 mg ml<sup>-1</sup>, respectively, in Ca buffer G (2 mM Tris pH 8.0, 0.2 mM ATP, 0.5 mM DTT, 0.1 mM CaCl<sub>2</sub>) and stored at -80 °C. Lyophilized porcine brain tubulin, biotinylated tubulin, and rhodamine-labeled tubulin are purchased from Cytoskeleton (T240, T33P, TL590M). Porcine tubulin and biotinylated tubulin are suspended to 5 mg ml<sup>-1</sup> in

PEM-100 [100 mM PIPES (pH 6.8), 2 mM MgCl<sub>2</sub>, 2 mM EGTA] and stored at -80 °C. Rhodamine-labeled tubulin is suspended to 5 mg ml<sup>-1</sup> using a 1:10 ratio of rhodamine-tubulin:unlabeled-tubulin in PEM-100 and stored at -80 °C.

To crosslink actin filaments within co-entangled actin-microtubule composites, we incorporate biotin-NeutrAvidin crosslinker complexes prepared using well-established and validated protocols described previously.<sup>1,6,22</sup> Crosslinker complexes, tubulin dimers, and G-actin are added to PEM-100 supplemented with 1 mM ATP, 1 mM GTP, and 5 μM Taxol. To determine filament mobility within composites, 0.13 μM of Alexa-488-labeled actin filaments and rhodamine-labeled microtubules are added to the solution.<sup>18</sup> To inhibit photobleaching of labeled filaments, oxygen scavenging agents [4.5 mg ml<sup>-1</sup> glucose, 0.5% β-mercaptoethanol, 4.3 mg ml<sup>-1</sup> glucose oxidase, 0.7 mg ml<sup>-1</sup> catalase] are included. For optical tweezers measurements, 4.5 μm carboxylated microspheres (Polysciences, Inc.), coated with Alexa-488 BSA (ThermoFisher) to inhibit binding interactions with the filaments, are included. The final mixture is pipetted into a ~20 μl sample chamber made from a glass slide and coverslip separated by ~100 μm of double-stick tape and sealed with epoxy. To polymerize filaments and form the crosslinked network, the sample is incubated for 30 minutes at 37 °C. G-actin polymerizes into ~7 nm wide semiflexible actin filaments composed of two entwined protofilaments and has a persistence length of  $l_p \approx 10 \mu\text{m}$ . Microtubules form from tubulin dimers into 25 nm wide tubes with 12–13 protofilaments around with  $l_p \approx 1 \text{mm}$ .<sup>23</sup>

For all presented data, we fix the total protein concentration to 5.8 μM with an equimolar ratio of actin monomers to tubulin dimers. We vary the crosslinker concentration to examine actin crosslinker molar ratios of  $R = [\text{NeutrAvidin}]/[\text{G-actin}] = 0, 0.005, 0.01, 0.02, 0.04$  and 0.08 (Fig. 1A). The mesh sizes of the actin network and microtubule network within composites are  $\xi_A = 0.3/c_A^{1/2} = 0.85 \mu\text{m}$  and  $\xi_M = 0.89/c_T^{1/2} = 1.58 \mu\text{m}$ , respectively, where  $c_A$  and  $c_T$  are the concentrations of actin monomers and tubulin dimers in units of mg ml<sup>-1</sup>.<sup>24–26</sup> The effective composite mesh size is  $\xi_C = (\xi_M^{-3} + \xi_A^{-3})^{-1/3} = 0.81 \mu\text{m}$ .<sup>6,18</sup>

The optical trap we use in all microrheology measurements (Fig. 1B and C), described and validated elsewhere,<sup>1,18</sup> is formed from an Olympus IX71 fluorescence microscope outfitted with a 1064 nm Nd:YAG fiber laser (Manlight) and 60× 1.4 NA objective (Olympus). A position-sensing detector (First Sensor) measures the deflection of the trapping laser which is proportional to the force acting on a trapped microsphere.<sup>27,28</sup> For all force measurements, a nanopositioning piezoelectric stage (Nano-PDQ, Mad City Labs) is used to move an optically trapped microsphere relative to the sample chamber while the laser deflection and stage position are recorded at 20 kHz. For oscillatory strain measurements the trapped sphere is sinusoidally displaced over an amplitude of 1 μm at frequencies of  $\omega = 1.26\text{--}138 \text{ rad s}^{-1}$ . For constant speed micro- and mesoscale strains, the trapped microsphere is displaced 5 or 10 μm at constant speeds of  $v = 1.25\text{--}20 \mu\text{m s}^{-1}$ . All displayed force curves and derived quantities are averages over >20 different trials taken in two different samples and in different

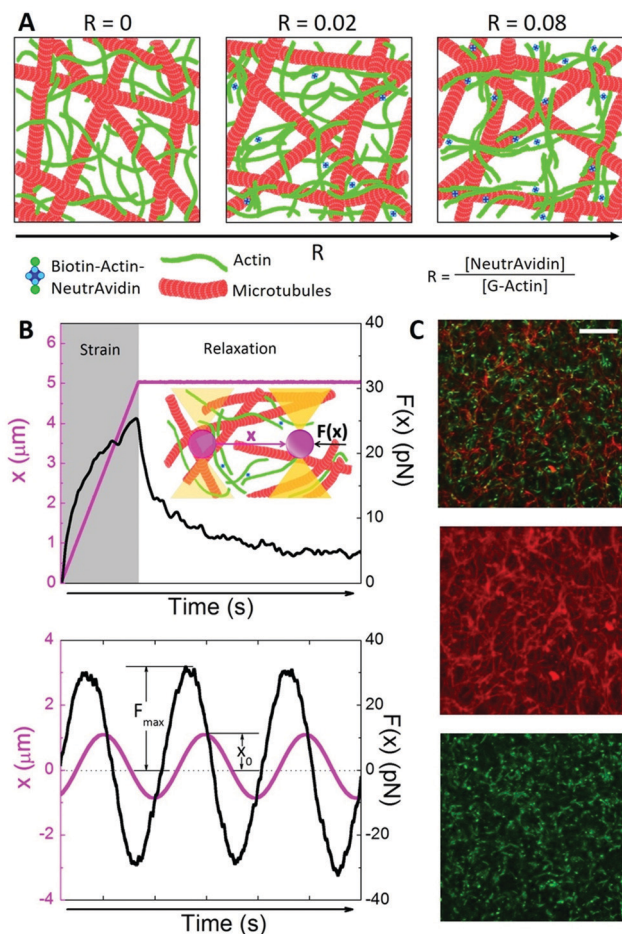


**Fig. 1** Experimental approach to characterize how actin crosslinking tunes the mechanics and mobility of actin-microtubule composites. (A) Cartoons (not drawn to scale) of composites of actin (green) and microtubules (red) with increasing concentrations of actin crosslinkers (blue) defined as the actin crosslinker ratio  $R = [\text{NeutrAvidin}]/[\text{G-actin}]$ . (B) Micro-rheology measurements. (top) Sample mesoscale constant strain measurement showing the force  $F(x)$  (black) exerted on the microsphere by the composite during (strain, grey region) and after (relaxation, white region) the microsphere is displaced ( $x$ , pink) at constant speed. Displacements of 5 and 10  $\mu\text{m}$  at speeds  $v = 1.25\text{--}20 \mu\text{m s}^{-1}$  are executed. Inset: Cartoon of measurement. (bottom) Sample microscale oscillatory strain measurement showing the force  $F(x)$ , black) exerted on a microsphere as it is sinusoidally oscillated ( $x$ , pink) through the composite. The force amplitude  $F_{\text{max}}$  and stage amplitude  $x_0$  are used to determine the complex viscosity  $\eta^*(\omega)$  as a function of frequency  $\omega$ . (C) (top) Two-color laser scanning confocal image of actin-microtubule composite with  $R = 0.08$ . For visualization of filaments,  $\sim 3\%$  of actin and microtubules are labeled with Alexa-488 (green) and rhodamine (red channel) respectively. (middle, bottom) Standard deviation projections of a 60 s video taken at 1 fps for the actin (green) and microtubule (red) channels. Scale bar is 25  $\mu\text{m}$ .

regions of the sample chamber, each separated by  $>100 \mu\text{m}$ , for each sample.

From average oscillatory strain force and stage position curves, we measure the amplitude of the oscillatory force curves  $F_{\text{max}}$ , as well as the amplitude of the stage position  $x_0$ , for each frequency  $\omega$  (Fig. 1B). As displayed in Fig. 2A we compute the complex viscosity *via*  $\eta^*(\omega) = F_{\text{max}}/6\pi x_0 \omega a$ ,<sup>29,30</sup> where  $a$  is the microsphere radius. From the constant speed force curves we

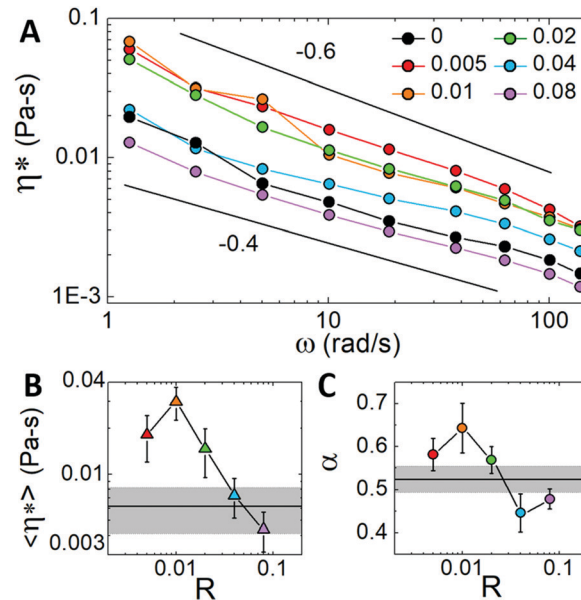


**Fig. 2** Viscosity and shear-thinning display non-monotonic dependence on  $R$  with values that are lower than unlinked composites for the highest  $R$  values. (A) Complex viscosity  $\eta^*(\omega)$  as a function of frequency  $\omega$  for varying  $R$  values shown in legend. Black lines show power-laws  $\eta^* \sim \omega^{-\alpha}$  with exponents listed. (B) The frequency-averaged viscosity *versus*  $R$  with black line and grey panel indicating the  $R = 0$  average and error. (C) Shear-thinning exponent  $\alpha$  *versus*  $R$  with black line and grey panel indicating  $\alpha$  for  $R = 0$ . As shown, viscosity and shear-thinning exponents increase with increasing  $R$  until  $R = 0.01$  after which they decrease to values that are below that for  $R = 0$  at  $R = 0.08$ .

compute an effective strain-averaged differential modulus *via*  $\langle K \rangle = \langle dF/dx \rangle$  where  $K$  is averaged over the entire strain or an otherwise specified region of the force curve.

To determine filament mobility, we use a Nikon A1R laser scanning confocal microscope with a  $60\times 1.4$  NA objective and QImaging QICAM CCD camera to collect 2D time-series of composites. The microscope is outfitted with 488 nm and 561 nm lasers that simultaneously record separate images in the green and red channels to visualize Alexa-488-actin (green) and rhodamine-tubulin (red) (Fig. 1C). For each crosslinker ratio, 3–5 time-series of  $512 \times 512$  images (0.41  $\mu\text{m}$  per pixel) in each channel are recorded at 1 fps for 60 seconds for two different samples.

Using FIJI/ImageJ, each time-series channel (green and red) is separately analyzed to determine the mobility of actin and microtubules in the composites, as previously described.<sup>6,18</sup> In short, we create a single projection image of the standard deviation of each pixel over time. We calculate the average standard deviation over all pixels for each projection image to obtain a single standard deviation value for the entire time-series  $\langle \delta \rangle$ . This value represents the variation in intensity values for each pixel over time and is thus a measure of the extent to which filaments in the composite fluctuate over time. In order to account for differences in the overall intensity among different time-series, we normalize each standard deviation value by the average intensity over all pixels and frames for each time-series ( $I$ ).

The resulting metric,  $\langle \delta \rangle / \langle I \rangle$ , quantifies the mobility of actin and microtubules in each time-series.

## Results and discussion

To investigate the role that actin crosslinking plays in cytoskeleton composites, we use previously established protocols to create co-entangled actin–microtubule composites in which we systematically tune the density of actin crosslinking.<sup>18,22</sup> We use biotin–NeutrAvidin as the crosslinker to create permanent actin-specific crosslinks devoid of transient unbinding/rebinding events, and we vary the actin crosslinker ratio from  $R = 0$  to  $R = 0.08$  (Fig. 1, Methods).<sup>1</sup>

### Linear viscoelasticity

We first examine how crosslinking impacts the linear viscoelasticity of composites by applying oscillatory strains of frequencies  $\omega = 1.26$ – $138 \text{ rad s}^{-1}$  and evaluating the frequency-dependent complex viscosity  $\eta^*(\omega)$  (Fig. 2). Based on previous studies on crosslinked actin networks, we expect the complex viscosity to increase as more crosslinkers are introduced.<sup>1,9,12,31</sup> Surprisingly, we instead find a non-monotonic dependence over the entire frequency range, with the average viscosity increasing by a factor of  $\sim 5$  from  $R = 0$  to  $R = 0.01$  and then decreasing by a factor of  $\sim 7$  such that the composite with the most crosslinkers ( $R = 0.08$ ) actually has a lower viscosity than the composite with no crosslinking ( $R = 0$ ) (Fig. 2A and B). Further, we see that all composites exhibit shear thinning, *i.e.*  $\eta^* \sim \omega^{-\alpha}$ . To determine the thinning exponent  $\alpha$  we fit the data for each  $R$  value to a power-law function over the entire frequency range displayed in Fig. 2A. As shown in Fig. 2C, we find that  $\alpha$  increases from  $\sim 0.52$  for  $R = 0$  to  $\sim 0.64$  for  $R = 0.01$ , after which it decreases to  $\sim 0.48$  for  $R = 0.08$ . Biopolymer solutions have been shown to display shear thinning with exponents of  $\sim 0.3$  to  $1$  depending on the extent of entanglement.<sup>32,33</sup> Our measured scaling exponents are within this range, so we likewise interpret higher scaling exponents as signifying increased network connectivity (Fig. 2C). As such, the non-monotonic dependence of  $\alpha$  on  $R$  suggests that introducing crosslinkers into composites initially increases network connectivity and viscoelasticity but, beyond a critical crosslinking ratio, crosslinkers serve to actually reduce connectivity. This counter-intuitive non-monotonic dependence is at odds with the majority of studies on crosslinked actin networks that show a monotonic increase in viscoelasticity and stiffness as  $R$  is increased.<sup>1,9,12,31</sup> The difference between prior studies and our work is the presence of microtubules, suggesting that the microtubules are the cause of this novel result.

### Nonlinear force response

To determine if this intriguing non-monotonicity persists in the nonlinear regime and at mesoscopic scales, we perform constant rate strain measurements for displacements of  $5$  and  $10 \mu\text{m}$  at constant speeds  $v = 1.25$ – $20 \mu\text{m s}^{-1}$  (Fig. 1B). Our previous work shows that the onset of the nonlinear regime for entangled actin–microtubule composites occurs at  $v_c \approx 5 \mu\text{m s}^{-1}$ ,<sup>18</sup> so we choose speeds that range from below to above this crossover.

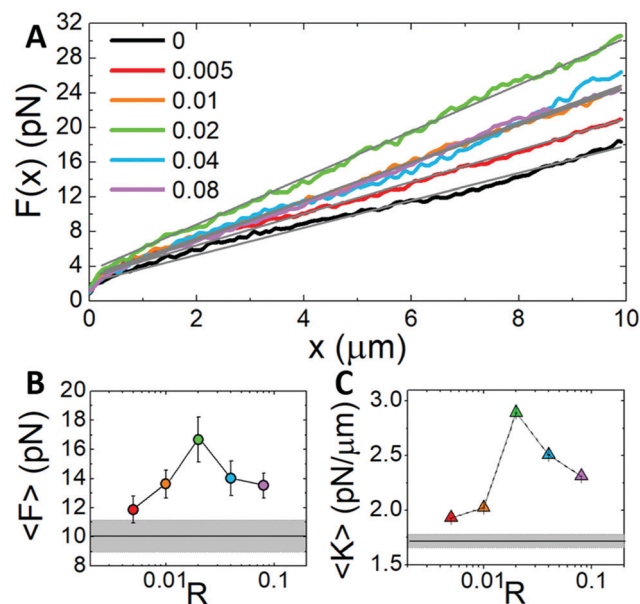


Fig. 3 Mesoscale force response of actin–microtubule composites shows non-monotonic dependence of stiffness on actin crosslinking. (A) Force  $F(x)$  composites exert to resist constant speed ( $v = 10 \mu\text{m s}^{-1}$ ) microsphere displacement  $x$  of  $10 \mu\text{m}$ . Grey lines are linear fits to the data from  $0.25$  to  $10 \mu\text{m}$ . (B) Average force over the full  $10 \mu\text{m}$  bead displacement with error bars denoting standard error across all trials. Colors match the legend in A and black line and grey panel are average and error for  $R = 0$ . (C) Average composite stiffness  $\langle K \rangle = \langle dF/dx \rangle$  determined from slopes of the linear fits shown in (A).  $R = 0$  is the solid line and grey panel.

Fig. 3A reveals the characteristic nonlinear force response that the composites exert to resist a  $10 \mu\text{m s}^{-1}$  displacement of  $10 \mu\text{m}$ . As expected, introducing crosslinkers increases the resistive force as all  $R > 0$  force curves are higher than the  $R = 0$  curve. However, similar to our unexpected viscosity data (Fig. 2), force curves do not monotonically increase with increasing  $R$ . Instead, we find that force curves increase from  $R = 0$  to  $R = 0.02$  and then decrease such that both  $R = 0.04$  and  $R = 0.08$  force curves are near that for  $R = 0.01$ . We quantify this non-monotonic dependence by calculating the average force over the strain ( $\langle F \rangle$ ) (Fig. 3B) which we find increases from  $\sim 10$  pN to  $\sim 17$  pN as  $R$  increases to  $0.02$ , before smoothly decreasing to  $\sim 13$  pN at  $R = 0.08$ .

However, as seen in Fig. 3A, not only does the magnitude of the force response depend on  $R$ , but the slope, which signifies the stiffness, depends on  $R$  as well. To evaluate the dependence of stiffness on  $R$  we compute the effective differential modulus  $K = dF/dx$ , *i.e.* the instantaneous slope of  $F(x)$ . Larger  $K$  values indicate stiffer more elastic composites while softer more viscous networks have smaller  $K$  values. All curves appear to have a very brief initial microscale response with a larger slope that transitions to a lower constant slope at  $\sim 0.25 \mu\text{m}$ . The constant slope indicates that  $K$  is nearly constant for the duration of the strain. As such, to evaluate the mesoscale stiffness we fit the force curves starting at  $0.25 \mu\text{m}$  to lines and equate the slopes to  $\langle K \rangle$ . As shown in Fig. 3C the dependence of  $\langle K \rangle$  on  $R$  exhibits the same non-monotonicity as the force response – initially

increasing with  $R$ , reaching a maximum for  $R = 0.02$ , followed by a decrease. We note that while both linear regime viscosity and nonlinear force and stiffness exhibit a non-monotonic dependence on  $R$ , the peak viscosity and peak nonlinear response are achieved at slightly different  $R$  values (0.01 vs. 0.02). We address this difference in the Discussion.

The non-monotonic dependence in the nonlinear regime is particularly surprising given the previously reported results for similar measurements performed on actin networks cross-linked with biotin–NeutrAvidin.<sup>1</sup> These studies showed that the average force and stiffness increase exponentially with  $R$  from  $R = 0$  to  $R = 0.07$ . Interestingly, these studies also reported that only the highest  $R$  values result in nearly elastic response (constant slope of  $F(x)$ ), compared to our results that show all networks maintaining a strong elastic response. The main difference between our data and this prior work is the presence of microtubules within the network. This result indicates that the differences in mechanical response must be due to the presence of microtubules within the network, highlighting the importance of the interactions between actin and microtubules in soliciting a unique force response for the composite material.

To connect the linear and nonlinear regime results and determine how the non-monotonicity that emerges in both regimes depends on strain speed we evaluate  $\langle F \rangle$  and  $\langle K \rangle$  as a function of speed for  $5 \mu\text{m}$  displacements (Fig. 4). As shown, the dependence of both  $\langle F \rangle$  and  $\langle K \rangle$  on  $R$  appear largely independent of speed, with all values increasing from  $R = 0$  to 0.01, after which they decrease, reaching a value lower than  $R = 0$  for  $R = 0.08$  for nearly all speeds.  $\langle F \rangle$  and  $\langle K \rangle$  also both display a speed dependence that is independent of  $R$  (Fig. 4). For both quantities, a shift in the speed dependence is observed above and below the nominal critical nonlinear speed of  $v_c \approx 5 \mu\text{m s}^{-1}$ .

To shed light on this speed dependence we fit our  $\langle F \rangle$  vs.  $v$  data to power-law functions for  $v \leq v_c$  and  $v \geq v_c$ . We find average scaling exponents of  $\sim 0.20$  for  $v \leq v_c$  compared to  $\sim 0.5$  for  $v \geq v_c$ . While the limited number of data points for each region limits the quantitative accuracy of the exponents, we can still conclude that both exponents are unequivocally less than 1 and that the exponent for  $v \leq v_c$  is less than that for  $v \geq v_c$ . This result indicates that all networks undergo shear-thinning that is reduced in the nonlinear regime ( $v > v_c$ ). Namely,  $F \sim v^1$  for a Newtonian fluid whereas a viscoelastic shear-thinning fluid, in which  $\eta \sim v^{-\alpha}$ , exhibits  $F \sim v^{1-\alpha}$ . Thus, the measured scaling exponents qualitatively corroborate the viscosity data (Fig. 2) and suggest that shear-thinning is reduced in the nonlinear regime ( $> v_c$ ).

Conversely,  $\langle K \rangle$  increases rapidly with speed below  $v_c$ , increasing over an order of magnitude; while  $\langle K \rangle$  exhibits a very weak dependence on  $v$  for speeds above  $v_c$ . These results demonstrate that the strong stiffness and elasticity (Fig. 3) is unique to the nonlinear regime whereas the filaments can relax imposed stress on the timescale of the strain (thereby reducing  $\langle K \rangle$ ) for speeds in the nominal linear regime.

Despite several of the speeds being above  $v_c$ , the  $R$  dependence for all speeds is akin to the linear regime mechanics (Fig. 2).

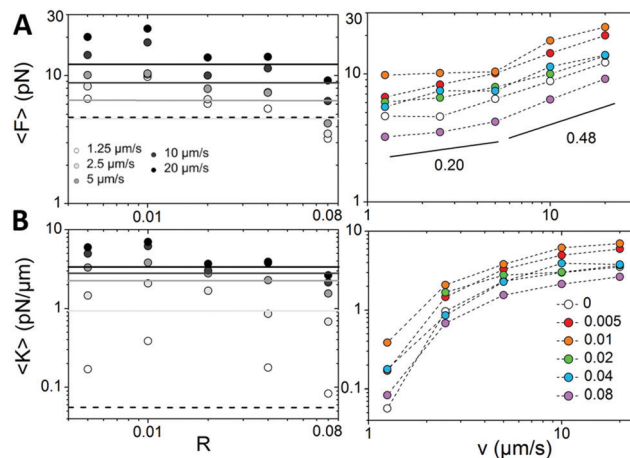
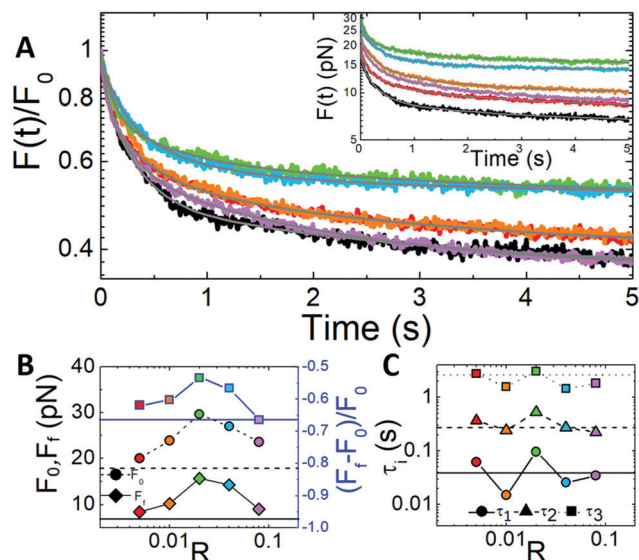


Fig. 4 The non-monotonic dependence of the force response on  $R$  persists for all strain speeds. The dependence of the average force  $\langle F \rangle$  (A) and stiffness  $\langle K \rangle$  (B) on the crosslinking ratio  $R$  (left) and strain speed  $v$  (right) for  $5 \mu\text{m}$  strains of  $v = 1.25, 2.5, 5, 10, 20 \mu\text{m s}^{-1}$ . The lines in left plots indicate  $\langle F \rangle$  and  $\langle K \rangle$  for the  $R = 0$  composite for each speed, matching colors in top left legend with the dashed line corresponding to  $1.25 \mu\text{m s}^{-1}$ . The different crosslinking ratios displayed in right plots are listed in the legend in (B). Black lines in  $\langle F \rangle$  vs.  $v$  plot correspond to power-laws with scaling exponents listed.

Namely, the peak values occur at  $R = 0.01$  rather than  $R = 0.02$ . The shift to  $R = 0.02$  for the peak in the  $10 \mu\text{m}$  strain (Fig. 3) must then be a result of the mesoscale strain distance rather than the high strain rate. We discuss the possible lengthscale-dependent source of this shift in the Discussion.

### Relaxation dynamics

The substantial stiffness and elasticity that composites exhibit in the nonlinear regime suggest that there should be limited dissipation following strain. Generally, we should expect to see the degree of strain memory (lack of dissipation) and the corresponding relaxation timescales to scale with the elasticity of the composite and thus exhibit a similar non-monotonic dependence. This scaling is exactly what is shown in Fig. 5, which displays the force relaxation following the mesoscale strain shown in Fig. 4. To quantify the dependence of dissipation on  $R$ , we plot the initial force  $F_0$  and final force  $F_f$  versus  $R$  (Fig. 5B). As shown, both  $F_0$  and  $F_f$  display the non-monotonic dependence we expect with  $R = 0.02$  exhibiting the highest value of each quantity. From these values we also compute the fractional force dissipation  $(F_f - F_0)/F_0$  which should be  $-1$  for complete dissipation and  $0$  for complete elastic memory. As shown in Fig. 5B, the fractional dissipation displays the expected non-monotonic dependence, reaching a maximum value of  $-0.53$  for  $R = 0.02$  and a minimum value of  $-0.66$  for both  $R = 0$  and  $R = 0.08$ . Thus, as indicated by our viscosity and force response results (Fig. 2 and 3), initially incorporating crosslinkers yields composites which are more elastic and thus exhibit increased resistivity and less relaxation over time. However, increasing the crosslinker ratio beyond  $R = 0.02$  yields softer more viscous composites with the  $R = 0.08$  composite exhibiting dissipation similar to the composite without crosslinkers.



**Fig. 5** The timescale over which composites dissipate force scales non-monotonically with crosslinking density. (A) Relaxation of force following strain  $F(t)$ , normalized by the force immediately following the strain  $F(t = 0) = F_0$ . Grey lines are fits to the exponential sum equation:  $F(t) = F_\infty + C_1e^{-t/\tau_1} + C_2e^{-t/\tau_2} + C_3e^{-t/\tau_3}$ . Inset shows un-normalized  $F(t)$  curves. (B) The initial force  $F_0$  (circles, dashed line for  $R = 0$ ), final force  $F_f$  (diamonds, solid line for  $R = 0$ ), and fractional force dissipation  $(F_f - F_0)/F_0$  (squares, solid blue line for  $R = 0$ ) vs.  $R$ . (C) Relaxation times determined from the fits shown in (A):  $\tau_1$  (circles, solid line for  $R = 0$ ),  $\tau_2$  (triangles, dashed line for  $R = 0$ ) and  $\tau_3$  (squares, dotted line for  $R = 0$ ). Colors match legend in Fig. 2–4.

While crosslinked composites do exhibit strong elastic features they still retain some degree of viscous dissipation as all composites relax induced force over time (*i.e.*  $F_f$  is always smaller than  $F_0$ ). We previously found that the force relaxation exhibited by crosslinked actin–microtubule composites following nonlinear strain was best described by a sum of three exponentials,  $F(t) = F_\infty + C_1e^{-t/\tau_1} + C_2e^{-t/\tau_2} + C_3e^{-t/\tau_3}$ , with the three time constants corresponding to distinct relaxation timescales and corresponding mechanisms.<sup>6</sup> Relaxations displayed in Fig. 5 are likewise well-fit to this function, with measured timescales that are all separated by an order of magnitude. These parameters once again display the non-monotonic dependence with  $R$  (Fig. 5C). Specifically, all three relaxation timescales reach a maximum at  $R = 0.02$  after which they decrease until reaching a value that is faster than the un-linked composite for  $R = 0.08$ .

To determine the relaxation mechanisms associated with each timescale, we compute the average of each over all  $R$  values –  $\tau_1 = 0.045 \pm 0.001$  s,  $\tau_2 = 0.318 \pm 0.007$  s, and  $\tau_3 = 2.23 \pm 0.09$  s – and compare to predicted relaxation modes for entangled actin filaments and microtubules. The fastest predicted timescale available to actin filaments is the mesh time  $\tau_m \approx \beta\zeta^4 l_p^{-1}$  where  $\beta = 1/k_B T$ ,  $\zeta$  is the translational friction coefficient, and  $\xi$  is the composite mesh size.<sup>6,34</sup> This timescale, associated with hydrodynamic effects of the surrounding composite (*i.e.* the time required for each filament to ‘feel’ its surroundings), is  $\sim 0.086$  s for our system,<sup>18,35</sup> which is comparable to our measured  $\tau_1$ . This agreement indicates that it is the relaxation of the actin filaments

within the composite, rather than the more rigid microtubules, that dictates the fast relaxation. This also makes sense physically, since rigid microtubules likely fluctuate more slowly than actin.

Another mechanism by which actin and microtubules are known to relax stress is *via* filament bending. The predicted timescale associated with bending is  $\tau_B \approx (\gamma/\kappa)[L/(3\pi/2)]^4$  where  $\kappa \approx l_p k_B T$  is the bending rigidity,  $L$  is the filament length,  $\gamma = (4\pi\eta_s/\ln(2\zeta/r))$  is the perpendicular drag coefficient,  $\eta_s$  is the solvent viscosity, and  $r$  is the filament radius.<sup>6,34,36</sup> Using our measured lengths for actin and microtubules in composites ( $L_A \approx 8.7$   $\mu\text{m}$  and  $L_M \approx 18.8$   $\mu\text{m}$ ) we compute bending times of  $\tau_{B,A} \approx 0.54$  s and  $\tau_{B,M} \approx 0.15$  s for actin and microtubules respectively. Both of these predicted values are similar to our average  $\tau_2$  value; however, the timescale for  $R = 0.02$  is much closer to  $\tau_{B,A}$  whereas for  $R = 0.08$  it is much closer to  $\tau_{B,M}$ . Thus, it may be the suppression of microtubule bending fluctuations that confer the strong elastic response seen for intermediate crosslinker ratios. We explore this possibility further below.

To determine the mechanism associated with the slowest measured relaxation times we look to previously reported relaxation timescales for actin networks crosslinked *via* biotin–NeutrAvidin.<sup>1</sup> This previous study reported two relaxation timescales that increase with increasing  $R$  ( $\tau_{\text{slow}} \approx 10\text{--}45$  s,  $\tau_{\text{fast}} \approx 0.8\text{--}1.8$  s) and are comparable to our slowest timescale  $\tau_3 \approx 2.23$  s. Both timescales are suggested to result from force-induced crosslinker unbinding and rebinding, which allows for slow reptation through entanglements ( $\tau_{\text{slow}}$ ) and fast lateral hopping between entanglement constraints ( $\tau_{\text{fast}}$ ).<sup>1,34,37</sup> Specifically, the applied strain forces crosslinks to temporarily unbind, allowing for the dominate mode of diffusion in entangled networks, reptation, to occur. However, nonlinear straining can also transiently decrease the entanglement density in the vicinity of the strain, which allows filaments to briefly escape from entanglement confinement and laterally ‘hop’ to a new confinement on a timescale much faster than reptation allows.<sup>1,38</sup> We can thus interpret our slowest relaxation timescale as arising from a combination of reptation and hopping, with the contribution from each depending on  $R$ . In composites with fewer crosslinks, reptation can occur without the need for unlinking, so we expect the contribution from reptation ( $\tau \sim O(10)$  s) to dominate over hopping ( $\tau \sim O(1)$  s). This is what we see for  $R = 0$  and  $R = 0.02$  composites: *i.e.*  $\tau_3$  is longer for  $R = 0$  and  $R = 0.02$  than those of  $R = 0.04$  and  $R = 0.08$  composites (Fig. 5C and 6C.) However, as  $R$  increases, free reptation is suppressed and unlinking is required for relaxation. The faster timescales for  $R = 0.04$  and  $0.08$  (faster than  $R = 0$ ) imply that while reptation is suppressed the filaments can easily hop between constraints. This result may also indicate that there are fewer constraints surrounding each filament that must be removed to be able to hop.

We next investigate the dependence of relaxation on strain speed (Fig. 6). The non-monotonic dependence of  $F_0$  and  $F_f$  is preserved for all speeds with the peak values (longest timescales) occurring at  $R = 0.01$ , and the values for  $R = 0.08$  actually being shorter than for  $R = 0$ . Further,  $F_0$  increases with increasing speed and exhibits a slight increase in scaling for  $\nu > \nu_C$  compared to  $\nu < \nu_C$  ( $F_0 \sim \nu^{0.19}$  vs.  $\nu^{0.41}$ ). Conversely,  $F_f$  decreases

with increasing speed for  $\nu < \nu_C$  ( $F_f \sim \nu^{-0.2}$ ), indicative of shear thinning, after which it is nearly independent of  $\nu$  ( $F_f \sim \nu^{0.08}$ ).

To determine if the relaxation mechanisms we measure for the mesoscale strain are rate-dependent we fit all relaxation curves to exponential functions. While relaxations following strains of  $\nu > \nu_C$  require the triple exponential function for proper fitting, with time constants that are similar to those shown in Fig. 5, curves for  $\nu < \nu_C$  are well fit to either single (for  $\nu = 1.25 \mu\text{m s}^{-1}$ ) or double (for  $\nu = 2.5 \mu\text{m s}^{-1}$ ) exponential functions. Specifically,  $\tau_1$  is not measured for either of the slower speeds, suggesting that the actin filaments can undergo this fast relaxation on the timescale of these strains. However, they all exhibit the slow relaxation timescale  $\tau_3$  indicating that reptation and hopping are required for relaxation in both linear and nonlinear regimes. As shown in Fig. 6C, the measured time constants for all speeds display the same non-monotonic dependence that the mesoscale relaxation curves exhibit (Fig. 5C). The independence of this result on speed corroborates that the

time constants indeed correlate with intrinsic relaxation mechanisms of the composites rather than strain-induced effects.<sup>39</sup>

### Filament mobility

To shed light on the filament fluctuations that may give rise to the non-monotonic stiffness we measure, we use dual-color confocal time-series to determine the steady-state mobility of both actin and microtubules within composites. As described previously<sup>6,24</sup> and in Methods, we quantify the mobility as the average standard deviation of the intensity over time for all pixels ( $\langle \delta \rangle$ ), normalized by the average intensity of all pixels over time ( $\langle I \rangle$ ) (Fig. 7). One would expect stiffer networks to correlate with reduced filament mobility, and actin crosslinking to suppress actin mobility more than microtubules (which remain unlinked for all  $R$ ). Fig. 7, which displays the mobility term  $\langle \delta \rangle / \langle I \rangle$  as a function of  $R$  for both actin and microtubules, shows that actin crosslinking reduces the magnitude and spread of the mobility of both filaments from that of the  $R = 0$  case. This result

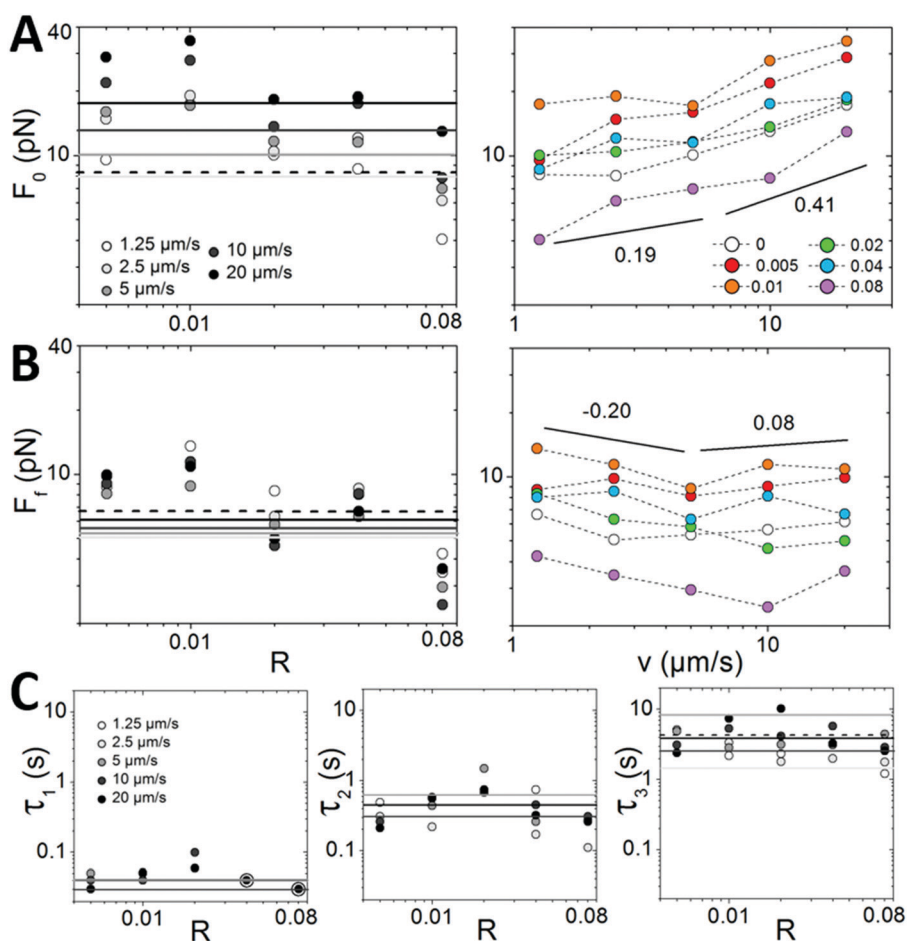


**Fig. 6** The degree of force dissipation and corresponding relaxation timescales exhibit non-monotonic dependence on  $R$  for all strain speeds. (A and B) The dependence of the initial force  $F_0$  (A) and final force  $F_f$  (B) on the crosslinking ratio  $R$  (left) and strain speed  $\nu$  (right) for  $5 \mu\text{m}$  strains of  $\nu = 1.25\text{--}20 \mu\text{m s}^{-1}$ . The lines in left plots indicate  $F_0$  (A) and  $F_f$  (B) for the  $R = 0$  composite for each speed, matching colors in top left legend with the dashed line corresponding to  $1.25 \mu\text{m s}^{-1}$ . The different crosslinking ratios displayed in right plots are listed in the legend in (A). Black lines in both plots correspond to power-laws with scaling exponents listed. (C) Time constants determined from the exponential fits to the force relaxation after  $5 \mu\text{m}$  strains of speeds listed in legend. The lines indicate  $R = 0$  for each speed matching scheme in top left plot. Large open circles in  $\tau_1$  plot indicate values obtained for  $R = 0.04$  and  $R = 0.08$  at  $20 \mu\text{m s}^{-1}$  which overlap with values obtained at  $10 \mu\text{m s}^{-1}$ .

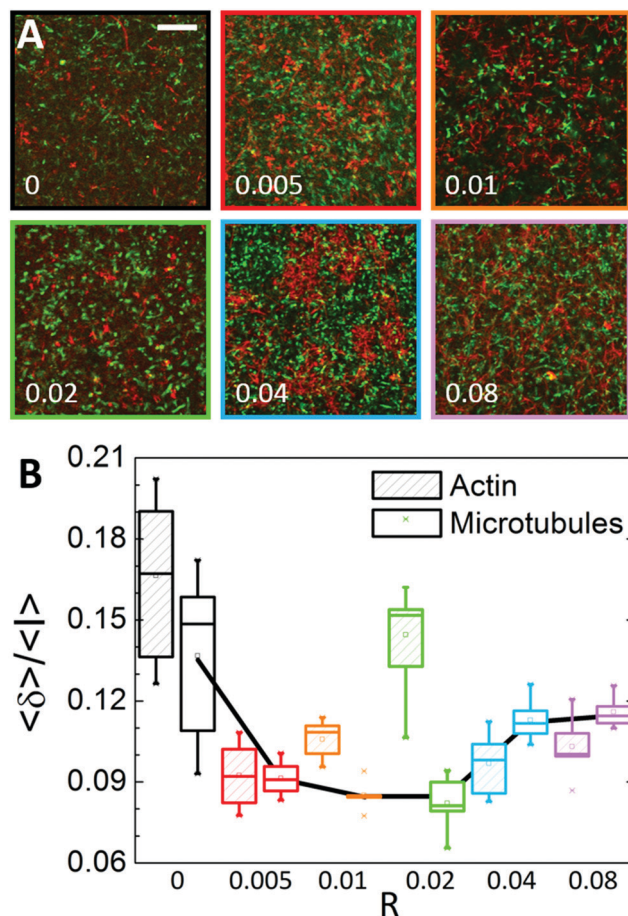


**Fig. 7** Microtubule mobility is tuned by actin crosslinking and dictates the non-monotonic mechanics of composites. (A) Projection images of the standard deviation of pixel intensity values in actin (green) and microtubules (red) channels for a 60 s time-series. Time-series are acquired using a Nikon A1R laser scanning confocal microscope with  $60\times 1.4$  NA objective. Numbers in bottom left of each image correspond to crosslinking ratio  $R$ . Colors outlining images match color scheme in (B). Scale bar is 25  $\mu\text{m}$ . (B) Box whisker plot of mobility calculated by computing the standard deviation of pixel intensities over time and space ( $\delta$ ), normalized by the average pixel intensity for each time-series ( $I$ ) as described in Methods. As shown, the mobility as well as the distribution of fluctuations for microtubules decreases until  $R = 0.02$  after which the mobility increases, with microtubules becoming more mobile than the actin filaments.

is intuitive as permanent crosslinking leads to stiffer more uniform networks with suppressed filament fluctuations and less heterogeneity. However, while stiffer composites do in fact confer reduced mobility, it is surprisingly the mobility of microtubules rather than actin that correlates with stiffness.

The mean magnitude of  $\langle \delta \rangle / \langle I \rangle$  for microtubules decreases from  $R = 0$  to  $R = 0.01$ , is nearly identical for  $R = 0.01$  and  $0.02$ , after which it increases with  $R$ . This non-monotonic dependence on  $R$ , which matches that of the mechanical properties presented above, suggests that the rigidity (*i.e.* reduced mobility) of the microtubules is the primary contributor to elasticity and stiffness. Crosslinking also reduces the mobility of actin, but surprisingly does not show the same clear trend as the microtubules. In fact, actin mobility shows no significant dependence

on the degree to which actin is crosslinked, with all distributions overlapping each other. Further, the highest mobility and largest spread (*i.e.* heterogeneity) in mobility is measured for  $R = 0.02$ , despite this network exhibiting the stiffest nonlinear mechanical response (Fig. 3).

Thus, while actin becomes more crosslinked as  $R$  increased, which should reduce its mobility, it appears that it is its ability to suppress microtubule mobility that controls the elasticity of the composite. This can be understood as actin filaments form a scaffolding network interwoven with the network of microtubules. As actin crosslinking increases the increased rigidity of the actin scaffold reduces the mobility of microtubules. Why then does the microtubule mobility and composite dissipation increase for  $R > 0.02$ ? We address this question below.

## Discussion

The robustness of the non-monotonic dependence of mechanics on  $R$ , and its coupling to microtubule mobility, requires a discussion of the mechanism leading to this surprising behavior. As depicted in Fig. 8, we suggest that as the crosslinking density increases beyond a critical density, actin filaments begin to form bundles, which increases the mesh size of the actin scaffold and reduces the connectivity between actin fibers (bundles or single filaments). This more loosely connected scaffold cannot as effectively suppress microtubule mobility as a denser network of individual crosslinked filaments. The distribution of individual force measurements for  $R = 0.08$  (Fig. 8) corroborates this interpretation. Namely, while the distribution of measured forces during strain are comparable to the  $R = 0$  case, there is a notable fraction of trials in which the optically trapped bead is forced out of the trap by the resistance of the composite (shown as points in Fig. 8C). This high-force response is what one would expect if the bead is forced against a region of well-connected actin bundles. Thus, while bundle connectivity (*via* crosslinking) is lower, resulting in the majority of force trials being comparable to that of  $R = 0$ , the regions in which bundles are well-connected lead to the large forces that pull the bead out of the trap. We note that our confocal images demonstrate that the networks at all  $R$  values remain isotropic and connected, without obvious signs of significant actin bundling. As such, the degree of bundling is likely on the order of a few filaments, such that a connected network still forms but with a larger mesh size and fewer connections than a network of individual crosslinked filaments. Our imaging methods are not sensitive enough to pick up these subtle microscale changes due to the high density and fluctuations of the labeled filaments.

To understand the slight difference in the  $R$  value at which peak elasticity is achieved for microscale and mesoscale strains ( $R = 0.01$  and  $0.02$  respectively), we examine the breadth of the mobility distributions for actin and microtubules at these crosslinking ratios. The distribution of microtubule mobility values is narrowest at  $R = 0.01$ , indicating that the scaffolding network is the most uniform and dense, such that microtubules in all regions of the network feel the same surroundings. The actin mobility distribution is likewise narrower than other

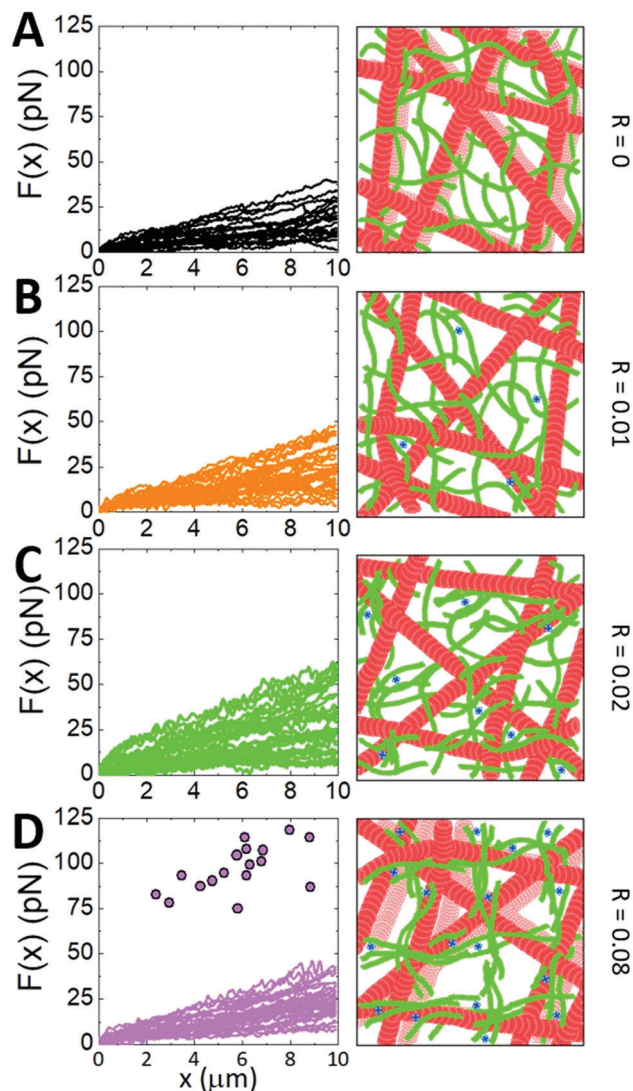


**Fig. 8** Higher crosslinker concentrations bundle actin filaments thereby increasing the mesh size and reducing the connectivity of the actin network scaffolding microtubules. Individual force measurements taken in different regions of the composite (left) and cartoons (not drawn to scale) of the effect of increasing crosslinking on the composite structure (right) for composites with crosslinker ratios  $R = 0$  (A),  $R = 0.01$  (B),  $R = 0.02$  (C) and  $R = 0.08$  (D). Cartoons depict mobility of microtubules as a translucent copy of each microtubule that represents its previous position. (A–C) The spread in the distribution of individual trials increases from  $R = 0$  to  $R = 0.02$  as the actin filaments go from un-linked ( $R = 0$ ) to crosslinked ( $R = 0.01$ ) to a heterogeneous mixture of crosslinked filaments and bundles ( $R = 0.02$ ). (D)  $R = 0.08$  composites exhibit two types of response: low force similar to  $R = 0$  and forces that are high enough that the microsphere is pulled out of the trap. Circles represent the force reached in trials in which the bead is pulled out. The two phases arise from bundling of the actin network that reduces the connectivity of the actin scaffold and creates sparse rigid regions where substantial bundling occurs (shown in cartoon in (D)).

$R$  values suggesting a uniformly crosslinked network. At  $R = 0.02$  the distributions for both actin and microtubules are larger than all other crosslinked ( $R > 0$ ) composites, suggesting that the composite is the most heterogeneous at this crosslinking density.

The actin mobility, in particular, displays a notably large spread in mobility values. A mixture of actin bundles and individual crosslinked actin filaments would provide the most heterogeneous scaffolding network, compared to scaffolds comprised solely of bundles or single filaments, owing to the wide distribution of actin mobility values.

This effect can also be seen in the larger distribution of measured force responses at  $R = 0.02$  compared to  $R = 0$  and  $0.08$  (Fig. 8). The increased mesh size that accompanies the onset of bundling (at  $R = 0.02$ ) serves to reduce the stiffness of the network at the microscopic scale as there are fewer network connections that the microsphere encounters. However, for mesoscopic strains, the effect of increasing mesh size is less significant and the increased rigidity of the actin bundles plays more of a role in the mechanical response. This mechanism would lead to a peak in stiffness at  $R = 0.01$  at the microscale and  $R = 0.02$  at the mesoscale.

We note that one previous study examining actin networks crosslinked by palladin reported a similar non-monotonic dependence in which actin networks appear to soften for very large  $R$  ( $> 0.1$ ).<sup>8</sup> Authors suggest that increased bundling at these high  $R$  values correspondingly increases the mesh size which gives rise to softer networks.<sup>8</sup> However, in this study the crosslinking density required to see such an effect is an order of magnitude larger than what we report and the effect is more subdued for the palladin result.

## Conclusions

Actin and microtubules are two key components that compose the cytoskeleton, and their interactions with one another enable critical cellular functions such as migration, apoptosis, neuronal pathfinding, *etc.* Actin crosslinking proteins add another tunable element to the composite cytoskeleton, enabling a wide range of viscoelastic properties needed for specific cell functions. While numerous studies have investigated the role of crosslinking on actin network mechanics, how actin-crosslinking tunes the composite cytoskeletal network of actin and microtubules remains an important unsolved problem.

Here, we directly address this open question by using optical tweezers microrheology and dual-color fluorescence confocal microscopy to reveal, for the first time, the surprising and diverse roles that actin crosslinking can play in the mechanical response and mobility of actin-microtubule composites. We create equimolar composites of co-entangled actin and microtubules with actin crosslinker ratios of  $R = 0$ – $0.08$ . We show that there is an unexpected and robust non-monotonic dependence of composite elasticity and filament mobility on  $R$  which persists from steady-state to nonlinear regimes and over micro- and mesoscopic scales. Specifically, we find that composite stiffness and relaxation timescales increase as  $R$  increases to  $R = 0.02$  as expected; however, increasing  $R$  further causes composites to exhibit increased dissipation and softer response, with  $R = 0.08$  appearing to be comparable to a composite with no crosslinkers present. We demonstrate that it is the synergistic interactions between actin and

microtubules that give rise to the emergent non-monotonicity which is largely absent in crosslinked actin networks (no microtubules). Specifically, the increased stiffness at intermediate crosslinking arises from a second order effect of actin crosslinking and bundling modulating microtubule mobility, which in turn dictates the composite elasticity.

Our results demonstrate the unique and complex ways that components of the composite cytoskeleton – such as actin, microtubules, and crosslinkers – work in concert to tune the mechanical properties of the cell over a wide parameter space with modest changes to the interactions between constituents. Moreover, our platform and results provide design principles for biomimetic materials with physical properties that can be precisely altered by varying the degree of crosslinking.

## Conflicts of interest

There are no conflicts to declare.

## Acknowledgements

This research was funded by a National Science Foundation CAREER Award (grant no. 1255446, awarded to R.M.R.-A.); a National Institutes of Health R15 Award (National Institute of General Medical Sciences Award No. R15GM123420, awarded to R.M.R.-A.); and a William M. Keck Foundation Research Grant (awarded to R.M.R.-A., J.L.R., M.D., and M.J.R.)

## References

- B. Gurmessa, S. Ricketts and R. M. Robertson-Anderson, *Biophys. J.*, 2017, **113**, 1540–1550.
- A. C. Murphy and P. W. Young, *Cell Biosci.*, 2015, **5**, 1–9.
- P. A. Janmey, *Proc. Natl. Acad. Sci. U. S. A.*, 2001, **98**, 14745–14747.
- Y. C. Fontela, H. Kadavath, J. Biernat, D. Riedel, E. Mandelkow and M. Zweckstetter, *Nat. Commun.*, 2017, **8**, 1981.
- A. N. Ketene, E. M. Schmelz, P. C. Roberts and M. Agah, *Nanomedicine*, 2012, **8**, 93–102.
- S. N. Ricketts, M. L. Francis, L. Farhadi, M. J. Rust, M. Das, J. L. Ross and R. M. Robertson-Anderson, *Sci. Rep.*, 2019, **9**, 12831.
- Y.-C. Lin, G. H. Koenderink, F. C. MacKintosh and D. A. Weitz, *Soft Matter*, 2011, **7**, 902–906.
- B. Grooman, I. Fujiwara, C. Otey and A. Upadhyaya, *PLoS One*, 2012, **7**, e42773.
- O. Lieleg, M. M. Claessens and A. R. Bausch, *Soft Matter*, 2010, **6**, 218–225.
- A. Bretscher, *Proc. Natl. Acad. Sci. U. S. A.*, 1981, **78**, 6849–6853.
- D. S. Courson and R. S. Rock, *J. Biol. Chem.*, 2010, **285**, 26350–26357.
- D. H. Wachsstock, W. Schwarz and T. Pollard, *Biophys. J.*, 1994, **66**, 801–809.
- C. P. Broedersz, M. Depken, N. Y. Yao, M. R. Pollak, D. A. Weitz and F. C. MacKintosh, *Phys. Rev. Lett.*, 2010, **105**, 238101.
- P. A. Janmey, S. Hvidt, J. Käs, D. Lerche, A. Maggs, E. Sackmann, M. Schliwa and T. P. Stossel, *J. Biol. Chem.*, 1994, **269**, 32503–32513.
- Y. Tseng, B. W. Schafer, S. C. Almo and D. Wirtz, *J. Biol. Chem.*, 2002, **277**, 25609–25616.
- Y. Tseng, T. P. Kole, J. S. Lee, E. Fedorov, S. C. Almo, B. W. Schafer and D. Wirtz, *Biochem. Biophys. Res. Commun.*, 2005, **334**, 183–192.
- E. Fuchs and I. Karakesisoglou, *Genes Dev.*, 2001, **15**, 1–14.
- S. N. Ricketts, J. L. Ross and R. M. Robertson-Anderson, *Biophys. J.*, 2018, **115**, 1055–1067.
- J.-Y. Sun, X. Zhao, W. R. Illeperuma, O. Chaudhuri, K. H. Oh, D. J. Mooney, J. J. Vlassak and Z. Suo, *Nature*, 2012, **489**, 133.
- J. Hu, K. Hiwatashi, T. Kurokawa, S. M. Liang, Z. L. Wu and J. P. Gong, *Macromolecules*, 2011, **44**, 7775–7781.
- S.-Z. Wu and M. Bezanilla, *J. Cell Biol.*, 2018, **217**, 3531–3544.
- S. N. Ricketts, B. Gurmessa and R. M. Robertson-Anderson, *Advances in Cytoskeleton Research*, IntechOpen, 2019.
- G. M. Cooper and R. Hausman, *The Cell*, Sunderland, MA, Sinauer Associates, 2nd edn, 2000.
- Y.-C. Lin, G. H. Koenderink, F. C. MacKintosh and D. A. Weitz, *Macromolecules*, 2007, **40**, 7714–7720.
- M. Gardel, M. Valentine, J. C. Crocker, A. Bausch and D. Weitz, *Phys. Rev. Lett.*, 2003, **91**, 158302.
- C. F. Schmidt, M. Baermann, G. Isenberg and E. Sackmann, *Macromolecules*, 1989, **22**, 3638–3649.
- M. C. Williams, *J. Cell Biol.*, 2002, **130**, 909–917.
- R. Brau, J. Ferrer, H. Lee, C. Castro, B. Tam, P. Tarsa, P. Matsudaira, M. Boyce, R. Kamm and M. Lang, *J. Opt. A: Pure Appl. Opt.*, 2007, **9**, S103.
- A. R. Bausch, W. Möller and E. Sackmann, *Biophys. J.*, 1999, **76**, 573–579.
- C. D. Chapman, K. Lee, D. Henze, D. E. Smith and R. M. Robertson-Anderson, *Macromolecules*, 2014, **47**, 1181–1186.
- R. Tharmann, M. Claessens and A. Bausch, *Phys. Rev. Lett.*, 2007, **98**, 088103.
- T. T. Falzone, S. Blair and R. M. Robertson-Anderson, *Soft Matter*, 2015, **11**, 4418–4423.
- C. D. Chapman, S. Gorczyca and R. M. Robertson-Anderson, *Biophys. J.*, 2015, **108**, 1220–1228.
- H. Isambert and A. Maggs, *Macromolecules*, 1996, **29**, 1036–1040.
- B. Gurmessa, R. Fitzpatrick, T. T. Falzone and R. M. Robertson-Anderson, *Macromolecules*, 2016, **49**, 3948–3955.
- F. Gittes, B. Mickey, J. Nettleton and J. Howard, *J. Cell Biol.*, 1993, **120**, 923–934.
- D. M. Sussman and K. S. Schweizer, *Macromolecules*, 2012, **45**, 3270–3284.
- Y. Yang, M. Bai, W. S. Klug, A. J. Levine and M. T. Valentine, *Soft Matter*, 2013, **9**, 383–393.
- M. Khan, K. Regan and R. M. Robertson-Anderson, *Phys. Rev. Lett.*, 2019, **1**, 013016.